ELSEVIER

Thin Solid Films 401 (2001) 216–224

thin solid films

www.elsevier.com/locate/tsf

Optical characterisation of anatase: a comparative study of the bulk crystal and the polycrystalline thin film

T.M.R. Viseu[a,*], B. Almeida[a], M. Stchakovsky[b], B. Drevillon[b], M.I.C. Ferreira[a], J.B. Sousa[c]

[a]*Centro de Física, Instituto de Materiais, Universidade do Minho, 4 700-320 Braga, Portugal*
[b]*Laboratoires des Couches Minces, École Polytechnique LPICM, CNRS–UMR 7 647, 91 128 Palaiseau, France*
[c]*Departamento de Física, IFIMUP, Universidade do Porto, R. Campo Alegre 687, 4 169-007 Porto, Portugal*

Received 28 December 2000; received in revised form 30 July 2001; accepted 6 August 2001

Abstract

The optical parameters of crystalline anatase and polycrystalline anatase films prepared by reactive magnetron sputtering were examined by spectroscopic ellipsometry and optical transmittance spectroscopy, respectively. Some films were doped with aluminium or chromium. In general, the values of the optical bandgap for the films are consistently blue-shifted as compared with the crystal. The blue shift is also found for some films doped with Al and Cr. The width of the absorption bands is considerably narrower in the films than in the crystal. These effects are interpreted as resulting from the spatial confinement of electrons and holes in the TiO_2 microcrystallites. The average crystallite size determined from the shift of the optical gap was found to be in the range ~5–8 nm, in excellent agreement with the data obtained from small-angle X-ray diffractometry.

Keywords: Titanium oxide; Optical properties; Quantum effects; Structural properties

1. Introduction

The successful application of anatase in novel dye-sensitised solar cells [1,2] and in the field of photocatalysis [3] has motivated numerous studies on the optical and electrical properties of this semiconductor, particularly in the form of a thin film [4–10].

Several theoretical studies on the structure and electronic properties of the rutile and anatase forms of TiO_2 have been reported [11–13]. More recently Mo and Ching [14] have published detailed theoretical studies on the electronic and optical properties of the three forms of titanium dioxide: rutile, anatase and brookite. However, only the rutile phase has been extensively studied experimentally from the point of view of its optical properties. In this respect, we refer the pioneering works of Cronemeyer [15] and Cardona and Harbeke [16]. Recently, some limited data on the optical properties of crystalline anatase have been obtained by Tang et al. [17]. This arises from the difficulty in obtaining clear synthetic monocrystals of anatase.

Moreover, the work reported by Tang et al. [18] on the optical and electrical properties of anatase and rutile films has shown that the main difference between both forms is the wider optical gap and the smaller electron effective mass of anatase compared to the other form. The possibility of doping these films [19] in the near future may become an efficient means to red shift the optical gap of this oxide towards the visible range of the solar spectrum.

Other publications on the optical characterisation of anatase films show that significant differences can be

* Corresponding author. Department of Physics, Campus de Gualtar, Minho University, 4 710-052 Braga, Portugal. Fax: +351-253 678 981.
E-mail address: tviseu@fisica.uminho.pt (T.M.R. Viseu).

0040-6090/01/$ - see front matter
PII: S0040-6090(01)01479-1

Table 1
Preparation conditions of TiO_2, TiO_2:Al and TiO_2:Cr thin films

	TiO_2					TiO_2:Al		TiO_2:Cr	
	T1	T2	T3	T4	T5	A1	A2	C1	C2
Substrate	Glass	Glass	Glass	Glass	Quartz	Glass	Glass	Glass	Glass
P_0 (Pa)	1.0×10^{-4}	2.5×10^{-4}	5.0×10^{-4}	1.0×10^{-4}	2.0×10^{-4}	1.8×10^{-4}	3.2×10^{-4}	1.0×10^{-3}	1.0×10^{-3}
$P(O_2)$ (Pa)	6.0×10^{-2}	6.0×10^{-2}	1.0×10^{-1}	5.0×10^{-2}	6.0×10^{-2}	6.0×10^{-2}	6.0×10^{-2}	6.0×10^{-2}	6.0×10^{-2}
$P(O_2+Ar)$ (Pa)	6.0×10^{-1}	6.0×10^{-1}	6.0×10^{-1}	6.0×10^{-1}	6.0×10^{-1}	6.0×10^{-1}	6.0×10^{-1}	6.0×10^{-1}	6.0×10^{-1}
Substrate temp. T (°C)	200	500	200	200	200	200	200	200	200
I(Ti) (A)	1.5	1.5	4.0	0.3	1.3	3.0	3.0	3.0	3.0
I(Al) (A)	–	–	–	–	–	0.25	0.02	–	–
I(Cr) (A)	–	–	–	–	–	–	–	0.22	0.16
% (Al or Cr)	–	–	–	–	–	2.1	Trace, <0.2	1.6	0.5
Deposition time t (min)	60	60	30	945	60	150	165	120	150
Deposition rate γ (nm/min)	7.5	7.8	16.6	0.7	3.4	5.4	5.3	3.5	3.8

found among films produced either by different techniques [20], or by the same technique, but under different preparation conditions [21,22].

In this work, we report on the preparation of anatase films by reactive magnetron sputtering. Some of the films were doped with aluminium or chromium. The optical parameters (n, k) of a high-purity natural crystal of anatase were measured by means of spectroscopic ellipsometry and compared with the theoretical calculations of Mo and Ching [14]. We also report on the optical parameters of each film in the range 200–2200 nm, with particular emphasis on the behaviour of the extinction coefficient, k, at the onset of the optical gap. The optical transmittance of each film was analysed by considering a detailed description of the film morphology that takes into account the characteristic dimension of the nanocrystalline domains, the presence of voids and the film roughness, in agreement with the data obtained from scanning electron microscopy, and high- and small-angle X-ray diffractometry. The effects of spatial confinement and doping on the optical properties of the films are discussed.

2. Experimental

2.1. Sample preparation

TiO_2 thin films were prepared by DC reactive magnetron sputtering in a commercial Alcatel system (model SCM 650) on glass and quartz substrates using a metallic Ti target of 99.9% purity. Doped films were prepared by co-sputtering. The preparation conditions are shown in Table 1.

The crystal aggregate used throughout originates from URI Mountains (Switzerland) and its purity was checked by electron microprobe analysis (EMA) in the energy dispersive mode, as shown in Table 2 (experiments performed at the Instituto Geológico e Mineiro, Porto, Portugal). The characteristic linear dimensions of the largest crystals are of the order of 6 mm. Two of the major crystals were cut parallel and perpendicular to the c axis of the crystalline structure by means of a diamond wheel, then fixed on a synthetic matrix and further polished. Crystal preparation was performed under the supervision of Prof Carlos L. Gomes, Department of Earth Sciences, University of Minho, whose assistance is duly acknowledged. Some of the minor crystals were reduced to powder and the anatase structure confirmed by X-ray diffractometry. The data are in excellent agreement with the standard parameters reported for this variety of TiO_2 [23], as shown in Fig. 1.

2.2. Sample characterisation

Scanning electron microscopy (SEM) of the films was performed in a Leica S360 system. The quantitative chemical composition of these samples was confirmed by an EMA system attached to the SEM equipment. High-angle X-ray diffractometry (HA-XRD) was per-

Table 2
Electron microprobe analysis (EMA) performed at eight different points of the crystal

	Crystal points (at.% of the metal oxide)							
	1	2	3	4	5	6	7	8
Al	0.00	0.00	0.00	0.00	0.00	0.00	0.00	0.00
Si	0.00	0.00	0.00	0.00	0.01	0.00	0.01	0.00
Ca	0.01	0.02	0.00	0.00	0.00	0.01	0.01	0.02
Ti	100.52	100.60	100.37	99.85	100.06	100.47	100.56	100.35
Fe	0.05	0.05	0.05	0.06	0.04	0.05	0.07	0.06
Sn	0.00	0.00	0.00	0.00	0.00	0.00	0.02	0.02

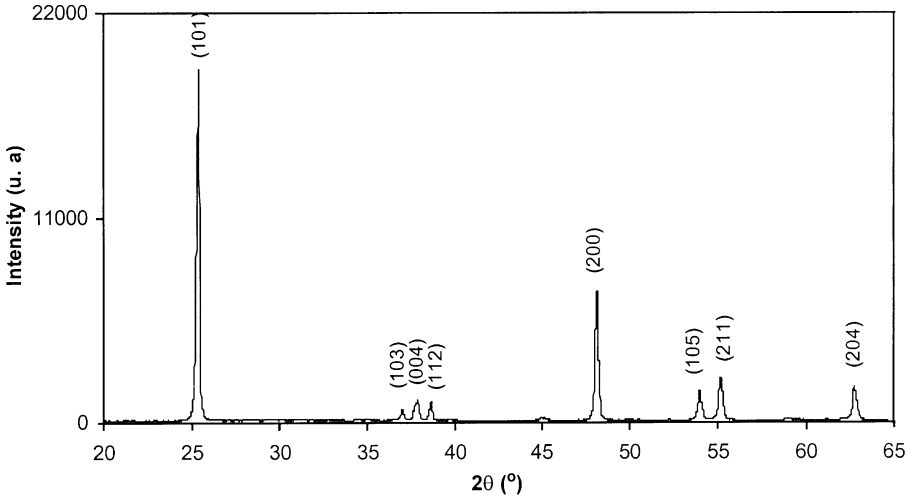

Fig. 1. High-angle X-ray diffraction (HA-XRD) pattern of the anatase crystal.

formed using a Philips PW 1710 diffractometer. Small-angle X-ray diffractometry (SA-XRD) was performed using a Siemens D5000 spectrometer. Optical transmittance spectra of the films were measured in a Shimadzu UV 3101 PC from 200 to 2200 nm. Spectroscopic ellipsometry measurements of crystalline anatase were performed using a UVISEL phase-modulated ellipsometer in the range 280–1700 nm.

3. Film structure and morphology

The SEM images shown in Fig. 2 display the characteristic columnar growth of materials prepared by sputtering, as well as the non-uniform film thickness.

Fig. 3a–c displays HA-XRD of non-doped, Al- and Cr-doped films prepared under the conditions summarised in Table 1. According to these data, all films show the structural features of anatase. The doped films display pronounced texture effects shown by the higher relative intensity of the (004) peak as compared to the T1 film. From the width of the main diffraction peaks and by means of the Scherrer formula, the coherence length of all films was found to be in the range 30–50 nm.

SA-XRD was performed under angles $2\theta \leq 10°$. In this way any micro-heterogeneity, such as voids, can be examined and characterised. Far from the critical angle of total reflection, the intensity of the diffracted beam (I) can be considered to be the sum of two independent contributions, one from the TiO_2 matrix (I_m) and the other from the pores or voids (I_p): $I = I_m + I_p$, where:

$$I_m = I_0 \left| \frac{r_{0,1} + r_{1,2}\, e^{2iqD}}{1 + r_{0,1}\ r_{1,2}\ e^{2iqD}} \right|^2 \quad (1)$$

$q = \frac{4\pi}{\lambda}\sin\theta$ is the wave vector, D is the film thickness, and $r_{i,j}$ are the Fresnel coefficients at the air–film and film–substrate interfaces [24].

The contribution from the pores was estimated according to the kinematic model of Mâaza et al. [25] by

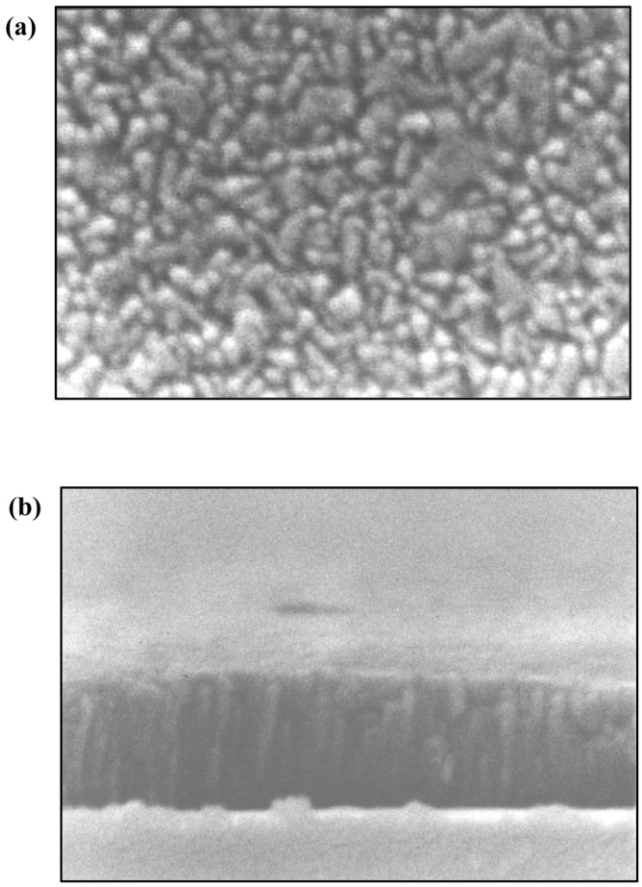

Fig. 2. Typical SEM images of a TiO_2 thin film: (a) surface and (b) cross-section.

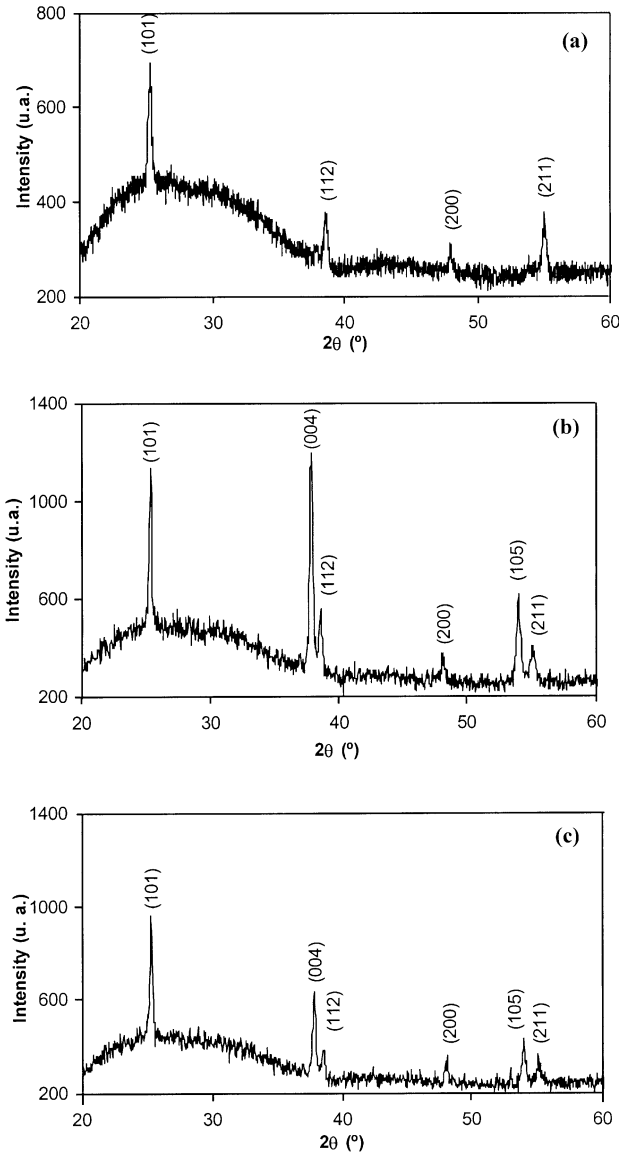

Fig. 3. High-angle X-ray diffraction (HA-XRD) patterns of TiO_2 thin films: (a) film T1; (b) film A1 (aluminium-doped); and (c) film C2 (chromium-doped).

considering each film to be composed of spherical voids (pores) randomly dispersed in a TiO_2 matrix. This model is particularly suited to study granular films. According to this model:

$$I_p = \zeta A^2(q) \times \left(\frac{1 - e^{-2q^2\sigma_s^2}}{1\text{-}2\cos(q\langle S_{ij}\rangle)e^{-q^2\sigma_s^2} + e^{-2q^2\sigma_s^2}} \right) \quad (2)$$

where:

$$A(q) = \frac{4}{3}\pi R^3 \left(\frac{\sin(qR) - qR\cos(qR)}{(qR)^3} \right) \times (\rho_{pores} - \rho_{matrix}) \quad (3)$$

ζ is a constant, proportional to the void concentration; $\langle S_{i,j}\rangle$ is the average inter-pore distance; $\sigma_s = S_{ij}$ is the

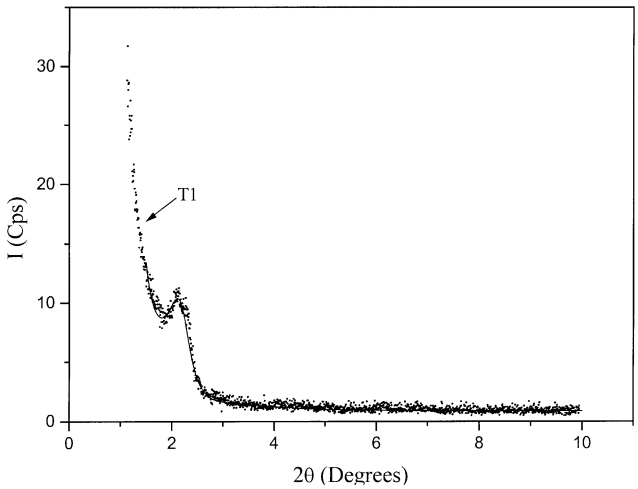

Fig. 4. Small-angle X-ray diffraction (SA-XRD) pattern of T1 film.

Gaussian distribution width; R is the pore radius; and ρ_{pores} and ρ_{matrix} are the electronic density of the pores and matrix, respectively.

The model also considers that the void size follows a Gaussian distribution, with an average pore radius $\langle R\rangle$ and width σ_R.

In the present work, the model of Mâaza et al. [25] was further improved by considering an interfacial roughness. This is equivalent to considering that the coefficients of Eq. (1) are replaced by effective ones, $r'_{i,j}$, with $\sigma_{i,j}$ the Gaussian distribution width of the average interfacial position:

$$r'_{0,1} = r_{0,1}e^{-q^2\sigma_{0,1}^2/2} \quad \text{and} \quad r'_{1,2} = r_{1,2}e^{-q^2\sigma_{1,2}^2/2}$$

In this work $\rho_{pores} \approx 0$, that is, all pores are considered spherical domains of near-zero electron density. Fig. 4 illustrates the fit of the model to the experimental curve of film T1. Table 3 summarises the results obtained for films T1, T3 and T4. The best fits were obtained for $\sigma_{0,1} \approx 2.5$ and $\sigma_{1,2} \approx 1.1$ nm. The dimensions of the voids, R, are found to be similar in all three films, whereas the estimated void fraction, f(v), of film T4 is significantly higher than the values of f(v) for both T1 and T3 films. This parameter, estimated here according to $f(\mathrm{v}) = \dfrac{(4/3)\pi\langle R\rangle^3}{\langle S_{ij}\rangle^3}$, will be further investigated in Section 4 of this work. The average distance calculated

Table 3
Fitted parameters from small-angle X-ray diffraction (SA-XRD)

	T1	T3	T4
$\langle R\rangle$ (nm)	1.87	1.95	1.96
σ_R (nm)	0.38	–	0.18
$\langle S_{i,j}\rangle$ (nm)	7.79	8.00	5.22
$\sigma_{Si,j}$ (nm)	0.79	–	1.10
f(v)	0.06	0.06	0.22

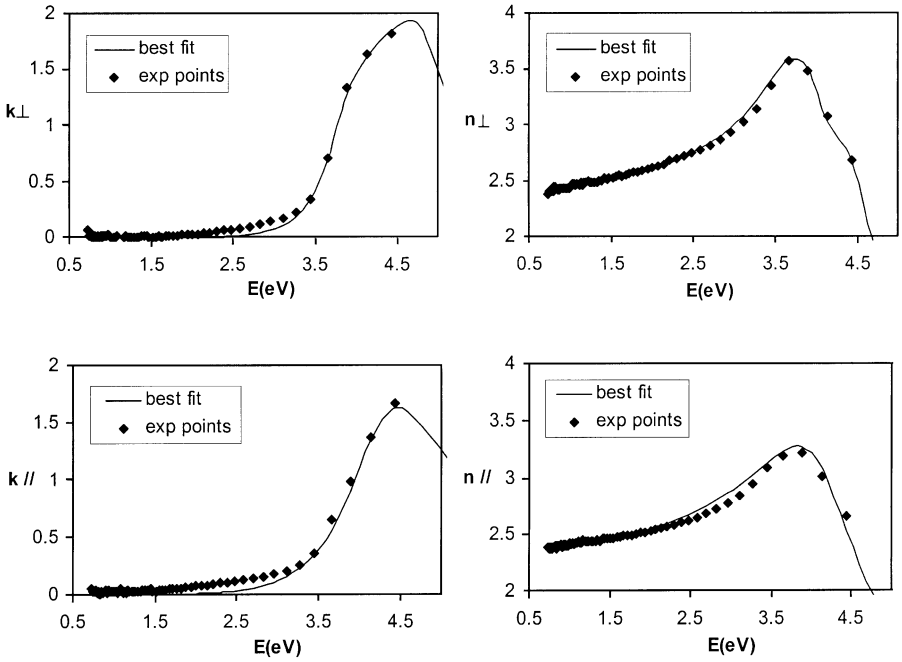

Fig. 5. Complex refractive index of the anatase crystal, measured by spectroscopic ellipsometry and adjusted by Forouhi and Bloomer treatment [26].

between pores, $\langle S_{ij}\rangle$, is considered to be a good indication of the average characteristic dimension of the microcrystalline domains. The values found for $\langle S_{ij}\rangle$ suggest that spatial confinement effects are to be expected, namely on the dielectric function of these films.

4. Optical studies

The behaviour of the dielectric constant of the crystal and all films was investigated by means of the unified treatment of Forouhi and Bloomer [26] applied to the optical range corresponding to the interband region of a solid, either crystalline or disordered.

The theoretical absorption coefficient, $\alpha = 2\omega k/c$, is defined considering all possible transitions from the valence to the conduction band of a solid. In this way, the extinction coefficient, $k(E)$, for the transition from state $|a\rangle$ to state $|b\rangle$, is determined from first-order time-dependent perturbation theory to be:

$$k = \Theta\frac{2\pi}{3}e^2\hbar^2\left|\langle b|\vec{x}|a\rangle\right|^2\frac{\gamma}{(E_0-E)^2+\frac{\hbar^2\gamma^2}{4}}$$

where: Θ is the number of possible transitions per unit volume in a layer of thickness $\Delta x \to 0$, $E_0 = E_b - E_a$, $\gamma = 1/\tau$ and τ is the finite lifetime of excited state $|b\rangle$.

By assuming a complete lack of momentum conservation, Θ will depend on the number of occupied states in the valence band and on the number of unoccupied

Table 4
Comparison of E_0 and E_g values obtained in this work with the predictions in [14]

	This work		Mo and Ching [14]	
	$\perp c$	$//c$	$\perp c$	$//c$
E_0 (eV)			3.0	
	3.92		3.8	3.8
	4.43	4.32	4.2	
			4.7	
			5.2	
E_g (eV)	2.0	1.5		
E_g (eV) (global)	2.00		2.04	

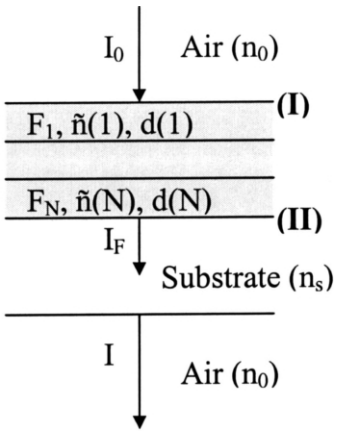

Fig. 6. Schematic representation of a multilayered thin film.

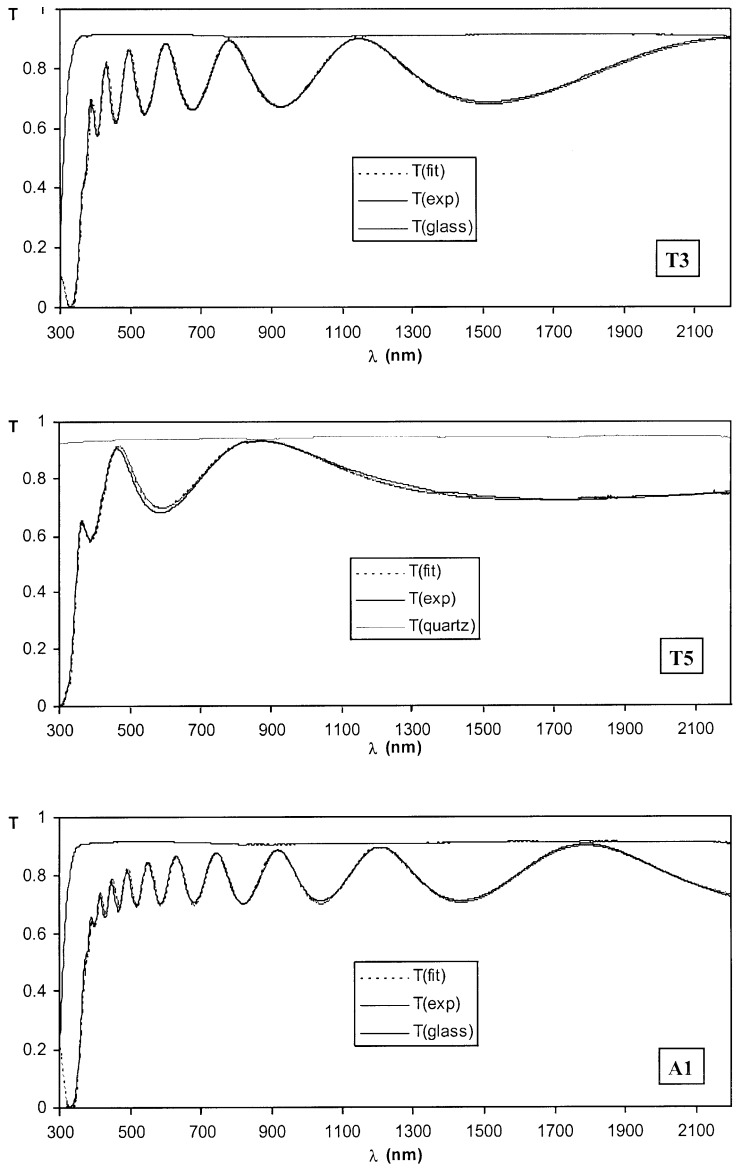

Fig. 7. Measured and calculated transmittance spectra of T3, T5 and A1 thin films.

states in the conduction band of the solid. Assuming further that valence and conduction bands are parabolic then:

$$\Theta = \text{const} \times (E - E_g)^2$$

where E_g is the optical energy bandgap, i.e. the energy at the onset of the fundamental interband absorption edge.

In the general case of the occurrence of several distinct interband transitions, $k(E)$ becomes:

$$k(E) = \left[\sum_i \frac{A_i}{(E - E_{0,i})^2 + \Gamma_i^2} \right] (E - E_g)^2 \quad (4)$$

and where $E_{0,i}$ is the energy corresponding to a maximum of the probability transition (k maximum).

Using the Kramers–Kronig relations, $n(E)$ is obtained analytically from $k(E)$:

$$n(E) = n(\infty) + \sum_i \frac{\rho_i (E - E_{0,i}) + \chi_i}{(E - E_{0,i})^2 + \Gamma_i^2} \quad (5)$$

and where:

$$\rho_i = \frac{A_i}{\Gamma_i} (\Gamma_i^2 - (E - E_g)^2)$$

and $\chi_i = 2 A_i \Gamma_i (E_{0,1} - E_g)$.

4.1. Optical studies on the crystal

The complex anisotropic refractive index of crystalline anatase was determined by means of spectroscopic

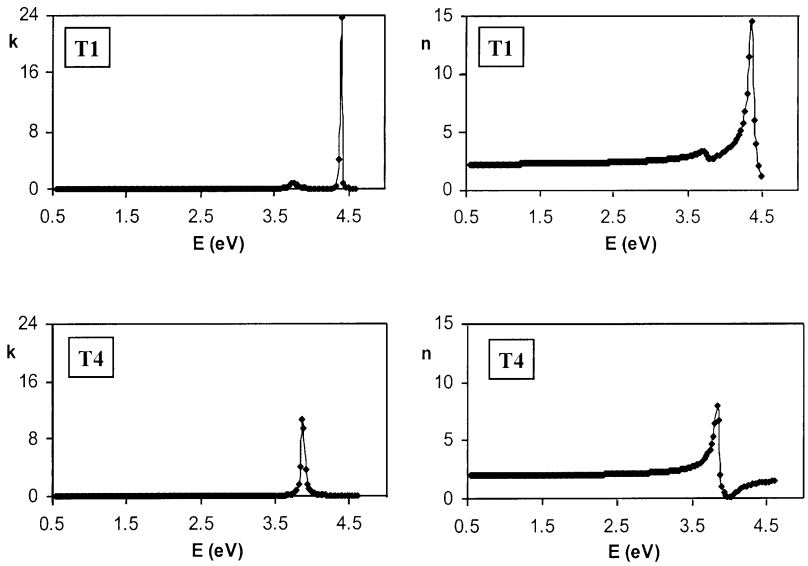

Fig. 8. Optical constants of films T1 and T4, calculated by the Forouhi and Bloomer treatment [26], using the parameters reported in Table 5.

ellipsometry in the range 0.75–4.5 eV. The experimental data and the best fits are plotted in Fig. 5. Significant optical anisotropy was found, in good agreement with the theoretical dielectric function calculated by Mo and Ching [14] from frequency-dependent interband optical conductivity in the dipolar approximation. By fitting the experimental data to the theoretical expressions Eqs. (4) and (5), it was possible to identify one maximum at 4.3 eV for $k(E)_{//}$, whereas two transitions could be resolved for $k(E)_{\perp}$ at 3.9 and 4.4 eV. The optical gap, E_g, was found to be 2.0 and 1.5 eV for $\perp c$ and $//c$, respectively. All the parameters are summarised in Table 4, with the corresponding theoretical values of Mo and Ching [14] also shown.

Good agreement is found, thus confirming the predictions of these authors that the band structure and density of states calculated for anatase are similar to rutile, in that both forms display the strong ionic character of the Ti–O bonds and strong hybridisation effects between O_{2p} and Ti_{3d} orbitals [11,14]. Moreover, the predicted value of $E_g = 2.04$ eV for a nearly direct gap is also in agreement with the value of 2.00 eV obtained in the present work for the crystal, since anatase displays uniaxial negative anisotropy, i.e. $a = b < c$ [27].

4.2. Optical studies on the films

The optical transmittance of each film was measured in the range 250–2200 nm (5.0–0.56 eV).

Analysis of the complete transmittance spectra was performed using the Abèles matricial model [28]. This model is particularly suitable for studying multilayered materials. In fact, the relationship between the electric and magnetic fields in interface (I), air/film F_1, and interface (II), film F_N/substrate, in a set of N optical layers, as schematically shown in Fig. 6, is

$$\begin{bmatrix} E_I \\ H_I \end{bmatrix} = \mathbf{M} \begin{bmatrix} E_{II} \\ H_{II} \end{bmatrix}$$

where $\mathbf{M} = \prod_{j=1}^{N} M_j$ is the characteristic matrix of the multilayered film, with

$$M_j = \begin{bmatrix} \cos\delta_j & i\dfrac{\sin\delta_j}{\tilde{n}_j} \\ i\tilde{n}_j \sin\delta_j \cos\delta_j & \end{bmatrix},$$

$$\delta_j = \frac{2\pi}{\lambda}\tilde{n}_j d_j \quad \text{and} \quad \tilde{n}_j = n_j - ik_j$$

The simulated transmittance curves (T_{calc}) were fitted to those measured (T_{exp}), and the best values of $n(E)$ and $k(E)$ for each layer were thus obtained. The void fraction, f(v), of each layer was taken into account by considering an effective refractive index, according to the effective medium approximation [29]. Film roughness, δ, was also considered by assuming a total film thickness $d_t = d \pm \delta$.

The spectra measured were analysed in a two-stage method. Firstly, it was assumed that $k(E) = 0$ and $\tilde{n}(E) = n(E)$ in the spectroscopic range 600–2200 nm, since all films are highly transparent in this spectroscopic region, as illustrated in Fig. 7. Application of the Abèles method has shown that the films prepared were optically homogeneous, i.e. equivalent to a single layer of finite porosity.

In the second stage, the experimental curves were analysed in the spectroscopic range 300–2200 nm according to the optical dispersion relations Eqs. (4)

Table 5
Parameters obtained from the best fit between transmittance spectra and the theoretical expressions of Forouhi and Bloomer [26], for TiO_2, TiO_2:Al and TiO_2:Cr thin films

	TiO_2						TiO_2:Al		TiO_2:Cr	
	Crystal	T1	T2	T3	T4	T5	A1	A2	C1	C2
d (nm)	–	446.88	468.26	498.12	643.07	204.05	810.36	872.24	424.60	568.43
δ (nm)	–	20.1	17.2	10.7	37.3	7.0	29.3	33.0	18.7	25.1
E_g' (eV)	2.00	2.1205	2.1025	2.0998	2.3490	1.9875	2.0134	2.0003	2.1802	2.3116
n_∞	2.105	2.0246	2.0394	2.0585	1.8830	1.8716	1.9152	1.8444	1.8349	1.9792
$E_{0,1}$ (eV)	3.942	3.758	3.755	3.736	3.867	3.804	3.723	3.816	3.868	3.742
A_1	0.0211	0.0012	0.0014	0.0024	0.0031	0.0008	0.0013	0.0019	0.0038	0.0018
Γ_1 (eV)	0.3375	0.0647	0.0646	0.1523	0.0237	0.1279	0.1270	0.0330	0.1078	0.0837
$E_{0,2}$ (eV)	4.493	4.403	4.505	4.496	–	4.422	–	–	–	4.432
A_2	0.126	0.0002	0.0001	0.0007	–	0.0059	–	–	–	0.0046
Γ_2 (eV)	0.808	0.0014	0.0013	0.0055	–	0.0938	–	–	–	0.0266
$E_{0,3}$ (eV)	–	–	–	–	–	5.289	5.042	5.354	5.232	–
A_3		–	–	–	–	0.0139	0.0003		0.0147	–
Γ_3 (eV)		–	–	–	–	0.3125	0.0026	0.1117	0.1290	–
φ	0.0610	0.0110	0.0105	0.0071	0.0110	0.0109	0.0070	0.0122	0.0059	0.0088
ΔE (eV) $\Delta E = Eg' - E_g^{crystal}$	–	0.1205	0.1025	0.0998	0.3490	≈0	0.0134	≈0	0.1802	0.3116
$2R_c$ (nm) (with $\mu = 0.2\ m_o$)	–	7.90	8.57	8.68	4.64	–	23.69	–	6.46	4.92
$\langle S_{i,j} \rangle$ (nm)		7.79		8.00	5.22					
f(v) (EMT)	–	0.129	0.109	0.079	0.266	0.155	0.119	0.174	0.183	0.121
γ (nm/min)	–	7.4	7.8	16.6	0.7	3.4	5.4	5.3	3.5	3.8

and (5) developed by Forouhi and Bloomer [26] under the following assumptions: (a) each film is formed by one optically homogeneous layer; and (b) each film has spherical voids randomly dispersed in bulk anatase. Excellent fits, as shown in Fig. 7, were obtained by assuming T_{calc} to be an average transmittance obtained from different film thickness values, in agreement with the assumed roughness, δ. The optical parameters of films T1 and T4 are shown in Fig. 8. The results obtained for all films studied are shown in Table 5. The quality of the fits was monitored by the residues, φ, defined as $\varphi = \left(\frac{\sum (T_{exp} - T_{calc})^2}{\sum (T_{exp})^2} \right)^{1/2}$.

Table 5 shows that it is possible to identify more than one interband transition energy in the films. In fact, in films T1–T3 and C2, two distinct optical transitions can be found in the regions 3.7–3.9 and 4.4–4.5 eV, corresponding to the transitions at 3.9 and 4.5 eV in the crystal, respectively (Table 4). Films T5, A1, A2 and C1 display another transition at 5.0–5.2 eV, which cannot be found in the crystal under our experimental conditions. However, it is interesting to note that the transition at ∼5 eV is predicted by the theoretical calculations of Mo and Ching [14].

The values found for the absorption bandwidths, $\Gamma_{0,i}$, in the films are substantially reduced compared to the corresponding parameter in crystalline anatase. In fact, for $E_{0,1}$ band $\Gamma_{0,1}$ varies from 0.024 eV in film T4 to 0.152 eV in film T3, whereas $\Gamma_{0,1} = 0.338$ eV in the crystal. The same feature is also found for the $E_{0,2}$ transition, but with more pronounced differences. The values of the optical gap for the films, E_g', are generally blue-shifted as compared to crystalline anatase. The higher values of the shift, $\Delta E = E_g' - E_g$, are found for T4 and C2 films.

These effects are ascribed to the spatial confinement of electrons and holes in the TiO_2 microcrystallites. Considering that both charge carriers are confined to rigid spherical crystallites, the bandgap of the confined material, E_g', is related to the bulk band gap, E_g, by [30]:

$$\Delta E = E'_g - E_g = \frac{\hbar^2 \pi^2}{2\mu R_c^2}$$

where $\mu = \frac{m_e m_h}{m_e + m_h}$ is the electron–hole pair effective mass and R_c is the crystallite radius. R_c values were obtained by considering the value of the Bohr radius of anatase proposed by Tang et al. [18]. These R_c values are in good agreement with the $\langle S_{ij} \rangle$ ones obtained by SA-XRD, thus confirming spatial confinement effects.

Moreover, the effective refractive index of all films, $n_{eff}(E)$, is lower than $n_{bulk}(E)$ measured for the crystal.

The estimated void fraction, $f(v)$, obtained from the effective medium treatment (EMT), is also shown in Table 5 for each film.

5. Conclusions

The optical parameters of nanocrystalline anatase thin films prepared by sputtering under controlled conditions were found to be in good agreement with the optical properties of crystalline anatase, as shown by the application of the unified treatment of Forouhi and Bloomer to the crystal and the films. The values of the optical gap for the films are, in general, blue-shifted in comparison to the crystal. Narrow absorption bands were found for the nanostructured films. These data are considered to be the result of quantum confinement effects, in accordance with the X-ray scattering data obtained in the small-angle configuration. Finally, the data indicate that higher confinement effects, i.e. smaller crystallites and higher porosity, are favoured by lower deposition rates.

References

[1] B. O'Reagan, M. Gratzel, Nature 335 (1991) 737.
[2] A. Kay, M. Gratzel, J. Phys. Chem. 97 (1993) 6272.
[3] E. Pelizzetti, M. Schiavello (Eds.), Photochemical Conversion and Storage of Solar Energy, Proceedings of the Eighth International Conference on Photochemical Conversion and Storage of Solar Energy, Kluwer Academic Publishers, 1991.
[4] M.H. Suhail, G. Mohan Rao, S. Mohan, J. Appl. Phys. 71 (1992) 1421.
[5] G.H. Li, L. Yang, Y.X. Jin, L.D. Zhang, Thin Solid Films 368 (2000) 163.
[6] G.P. Larivière, J.M. Frigerio, J. Rivory, F. Abèles, Appl. Opt. 31 (1992) 6056.
[7] S.Y. Kim, Appl. Opt. 35 (1996) 6703.
[8] M. Mosaddeq-ur-Rahman, G. Yu, K.M. Krishna, T. Soga, J. Watanabe, T. Jimbo, M. Umeno, Appl. Opt. 37 (1998) 691.
[9] R. Könenkamp, R. Henninger, P. Hoyer, J. Phys. Chem. 97 (1993) 7328.
[10] B. Enright, D. Fitzmaurice, J. Phys. Chem. 100 (1996) 1027.
[11] A. Fahmi, C. Minot, B Silvi, M. Causá, Phys. Rev. B 47 (1993) 11717.
[12] K.M. Glassford, J.R. Chelikowsky, Phys. Rev. B 46 (1992) 1284.
[13] N. Daude, C. Gout, C. Jouanin, Phys. Rev. B 15 (1977) 3229.
[14] S.D. Mo, W.Y. Ching, Phys. Rev. B 51 (1995) 13023.
[15] D.C. Cronemeyer, Phys. Rev. 87 (1952) 876.
[16] M. Cardona, G. Harbeke, Phys. Rev. 137 (1965) A1467.
[17] H. Tang, H. Berger, P.E. Schmid, F. Lévy, Solid State Commun. 92 (1994) 267.
[18] H. Tang, K. Prasad, R. Sanjinès, P.E. Schmid, F. Lévy, J. Appl. Phys. 75 (1994) 2042.
[19] P. Pichat, in: E. Pelizzetti, M. Schiavello (Eds.), Photochemical Conversion and Storage of Solar Energy, 1991, p. 277.
[20] J.M. Bennett, E. Pelletier, G. Albrand, J.P. Borgogno, B. Lazarides, C.K. Carniglia, R.A. Schmell, T.H. Allen, T.T. Hart, K.H. Guenther, A. Saxer, Appl. Opt. 28 (1989) 3303.
[21] J. Rodriguez, M. Gomez, J. Ederth, G.A. Niklasson, C.G. Grandqvist, Thin Solid Films 365 (2000) 119.
[22] L. Meng, M. Andritschky, M.P. Santos, Thin Solid Films 223 (1993) 242.
[23] JCPDS, International Center for Diffraction Data, Search Manual, File 21-1272, 1998.
[24] M. Born, E. Wolf, Principles of Optics, Pergamon Press, 1970.
[25] M. Mâaza, A. Gibaud, C. Sella, B. Pardo, F. Dunsteter, J. Corno, F. Bridou, G. Vignaud, A. Désert, A. Menelle, Eur. Phys. J. B 7 (1999) 339.
[26] A.R. Forouhi, I. Bloomer, Phys. Rev. B 34 (1986) 7018.
[27] M. Roubault, Détermination des Mineraux des Roches au Microscope Polarisant, Editions Lamarre, Paris, 1991.
[28] F. Abelès, Optics of Thin Films — Advanced Optical Techniques, Amesterdam, 1967, Chapter 5.
[29] I. Webman, J. Jortner, M.H. Cohen, Phys. Rev. B 15 (1977) 5712.
[30] H. Haug, S.W. Koch, Quantum Theory of the Optical and Electronic Properties of Semiconductors, 3rd, World Scientific Publishing Co, 1990.